RSC Advances

PAPER

View Article Online
View Journal | View Issue

Cite this: *RSC Adv.*, 2023, **13**, 19039

Enhanced stability and tunable photoluminescence in Mn^{2+}-doped one-dimensional hybrid lead halide perovskites for high-performance white light emitting diodes†

Jie Zhang,[ab] Kai-Qi Sun,[b] Zhong-Hui Zhang,[b] Ri-Cheng Wang,[b] Zi-Han Lin,[b] Xiao-Wu Lei,[b] Yu-Yin Wang,*[b] Ping Ju[a] and Yuan-Chun He*[a]

Organic–inorganic hybrid low-dimensional lead halides have garnered significant interest in the realm of solid-state optical materials due to their unique properties and potential applications. In this study, we report the synthesis, characterization and application of Mn^{2+}-doped one-dimensional (1D) [AEP] $PbCl_5 \cdot H_2O$ hybrid lead halide perovskites with tunable photoluminescence properties. The Mn^{2+} doping leads to a redshift of the dominant emission wavelength from 463 nm to 630 nm, with the optimal doping concentration resulting in an enhanced photoluminescence quantum yield (PLQY) from less than 1% to 8.96%. The structural and optical stability of these doped perovskites have been thoroughly investigated revealing excellent performance under humid and high-temperature conditions. Perovskite–PVP composite films exhibit high crystallization and bright orange-red emission under UV excitation. Furthermore, we demonstrate the successful fabrication of a white LED device using the Mn^{2+}-doped perovskite in combination with commercial green and blue phosphors. The fabricated LED exhibits a high color rendering index (CRI) of 87.2 and stable electroluminescence performance under various operating currents and extended operation times. Our findings highlight the potential of Mn^{2+}-doped 1D hybrid lead halide perovskites as efficient and stable phosphors for high-performance white light emitting diodes and other optoelectronic applications.

Received 28th April 2023
Accepted 19th June 2023

DOI: 10.1039/d3ra02813e

rsc.li/rsc-advances

Introduction

Lead trihalide-based three-dimensional (3D) perovskite materials ($APbX_3$, A = Cs^+, methylammonium; X = Cl, Br, I) have garnered significant research interest for various optoelectronic devices, including high-efficiency solar cells, color-tunable and narrow linewidth light-emitting diodes (LEDs), lasers, and photodetectors.[1–8] These materials represent a new paradigm for renewable energy sources due to their exceptional charge carrier mobilities, low density of midgap trap states, and defect-tolerant nature. Furthermore, 3D $APbX_3$-based materials offer potential applications in solid-state lighting and display technologies, owing to their attractive optical properties, such as high PLQY, tunable bandgaps, emission wavelengths spanning the entire visible spectrum, narrow linewidths and rapid radiation decay rates.[9–12] Nonetheless, 3D perovskites have some remaining drawbacks including moisture absorption, water decomposition, and limited thermal stability, which impede their use in optoelectronics. Low-dimensional hybrid metal halide perovskites present an alternative to 3D perovskites, offering benefits such as tunable emission wavelength, enhanced PLQY, improved moisture resistance, and thermal stability.[13–22]

The numerous advantages of low-dimensional perovskites have driven researchers to optimize their luminescent properties through various modulation strategies. Among these, replacing lead with non-toxic metal ions has emerged as a promising approach for tuning photoluminescent properties.[23–28] Metal ions such as Mn^{2+}, Zn^{2+}, Cd^{2+}, and rare earth ions have successfully replaced some Pb ions, with Mn^{2+} being particularly attractive due to its high luminescence efficiency and non-toxicity.[29–34] Mn^{2+} doping has been extensively studied in 0D, 2D, 3D and bimetallic perovskites showcasing great potential for optoelectronic device applications like light-emitting diodes, thanks to their enhanced stability and exciton binding energy. Recent research has demonstrated the successful incorporation of Mn ions into lead perovskite nanocrystals, revealing the influence on energy transfer

[a]College of Chemistry and Chemical Engineering, Qufu Normal University, Qufu, Shandong, 273165, P. R. China. E-mail: heyc240@nenu.edu.cn

[b]Department of Chemistry and Chemical Engineering, Jining University, Qufu, Shandong, 273155, P. R. China. E-mail: wangyuyin66@163.com

† Electronic supplementary information (ESI) available: Experimental, theoretical, analytical and crystallographic details. CCDC 2252459. For ESI and crystallographic data in CIF or other electronic format see DOI: https://doi.org/10.1039/d3ra02813e

between the Mn ion and semiconducting host. The successful single-site synthesis of colloidal Mn-doped cesium halide lead perovskite nanocrystals has resulted in intensive Mn^{2+} associated luminescence, suggesting that $CsPbX_3$ nanocrystals could serve as a novel platform for magnetically doped quantum dots.[35–37] These achievements in 3D perovskites inspire us to employ similar methods to optimize the luminescent properties of low-dimensional perovskites.

Liu and colleagues introduce a novel family of doped nanocrystals (NCs) that offer valuable insights into the chemical mechanisms of doping and the fundamental interactions between dopant and semiconductor hosts. Specifically, they have developed an effective method for incorporating Mn ions into lead halide perovskite NCs by examining the role of relative bond strengths within the lattice of precursors and hosts. They observed a striking impact of halide properties on the relative strength of intrinsic band edges and Mn emission bands, which they attribute to the effect of the energy difference between corresponding transitions on the energy transfer properties between the Mn ion and the semiconductor host.[38]

David and his colleagues report the single-site synthesis of colloidal Mn-doped cesium halide lead ($CsPbX_3$) perovskite NCs, resulting in effective intraparticle energy transfer between excitons and dopant ions, leading to intense sensitized Mn luminescence. At a doping concentration of 0.2%, the Mn-doped $CsPbCl_3$ and $CsPb(Cl/Br)_3$ nanocrystals retained the same lattice structure and crystallinity as their undoped counterparts, with nearly identical lattice parameters and no signs of phase separation. They found that $CsPbX_3$ NCs possess numerous superior optical and electronic properties, potentially serving as a new platform for magnetically doped quantum dots and extending the range of optical, electronic, and magnetic functions. The significant achievement of manganese doping in 3D perovskites inspired the researchers to adopt similar methods for optimizing the luminescence properties of low-dimensional perovskites.[39]

In this study, we synthesized a 1D bulk crystal $[AEP]PbCl_5 \cdot H_2O$ using the ambient temperature volatilization method, but the luminescence is extremely weak. To enhance the PLQY of this compound, we doped Mn^{2+} into the synthesized 1D bulk crystal. We found that the Mn^{2+}-doped 1D perovskite exhibited efficient and tunable broadband luminescence from the blue to red spectral range, with the highest PLQY reaching 8.96%. DFT calculation reveal that the energy transfer between the host lattice and Mn^{2+} ions, referred to as Förster Resonance Energy Transfer (FRET), plays a crucial role in the observed redshift. This energy transfer process involves the absorption of photons by the host lattice, followed by a non-radiative transfer of energy to the Mn^{2+} ions and then radiative recombination from Mn^{2+} center. Moreover, systematic studies revealed that these Mn^{2+}-doped perovskites demonstrated excellent structural and optical stability under both humid atmospheric and high-temperature conditions. This research not only deepened our understanding of the Mn doping strategy but also offered a novel approach for improving the luminescence performance of perovskite materials.

Experimental section

Materials

$PbCl_2$ (99.7%, Aladdin), HCl (37%, Aladdin), $MnBr_2 \cdot 4H_2O$ (Aladdin), 1-(2-aminoethyl)piperazine (99.9%, Aladdin). All chemicals were purchased and used without any further purification.

Synthesis of $[AEP]PbCl_5 \cdot H_2O$ (compound 1)

A mixture of $PbCl_2$ (0.5 mmol, 0.1391 g) and 1-(2-aminoethyl) piperazine (0.6 mmol, 0.08 g) was dissolved in 5 mL of HCl under vigorous stirring, followed by heating to 100 °C for approximately 5 minutes until a clear solution formed. The reactants were then cooled to room temperature at a cooling rate of 5 °C min^{-1}, and transparent crystals were obtained after maintaining the solution at room temperature for 5 days. The crystals were filtered from the solution and washed three times with ethanol, resulting in the colorless crystal of $[AEP]PbCl_5 \cdot H_2O$ with a yield of 45%. Elemental analysis calculations for $C_{12}N_6H_{38}OPb_2Cl_{10}$ showed C, 13.71%, N, 7.99%, H, 3.64%, while the obtained results were: C, 13.15%, N, 8.24%, H, 3.94%.

Synthesis of $[AEP]Pb_{1-x}Mn_xCl_5 \cdot H_2O$

To prepare a series of $[AEP]Pb_{1-x}Mn_xCl_5 \cdot H_2O$ phases (compound **2–9**), $MnCl_2 \cdot 4H_2O$ was used as the source of Mn^{2+} and doped into compound **1** using the above method. To rationally manage the doping concentration of Mn^{2+}, the Mn^{2+}/Pb^{2+} dosage ratio was continuously controlled from 0 : 1 to 20 : 1. The concentrations of dopant (manganese ions) in the $[AEP]Pb_{1-x}Mn_xCl_5 \cdot H_2O$ phases (compound **2–9**) are listed in Table S4.†

X-ray crystallography

Single-crystal X-ray diffraction data of $[AEP]PbCl_5 \cdot H_2O$ were collected using a Bruker D8 Quest diffractometer with graphite-monochromated Mo Kα radiation ($\lambda = 0.71073$ Å) at 293 K. The structure was solved and refined by the SHELXL-2018/3 program within OLEX2, with all atoms being refined with anisotropic atomic displacement parameters, except the H atoms, which were placed in idealized positions and allowed to ride on the relevant carbon atoms. Detailed crystal data and structural refinement for compound **1** are summarized in Table S1.† Selected bond lengths (Å) and bond angles (°) are listed in Table S2,† and hydrogen bond data are collected in Table S3.†

Characterization methods

The powder X-ray diffraction (PXRD) pattern was collected using a Rigaku MiniFlex II diffractometer, operating at 40 kV and 40 mA with Cu Kα radiation ($\lambda = 1.5406$ Å). The diffraction pattern was scanned over the angular range of 5–60° (2θ) with a step size of 5° min^{-1} at room temperature. Thermogravimetric analysis (TGA) was carried out using a Netzsch STA 449C thermal system, with samples heated from 35 to 800 °C at a rate of 20 °C min^{-1} under an N_2 atmosphere. Solid-state UV-vis optical absorption spectra were performed on a PE Lambda 900 UV-vis

spectrophotometer. X-ray photoelectron spectroscopy (XPS) spectra were tested using the Escalab XI+ instrument, USA. SEM and EDX images were obtained using the Hitachi SU-8010 field emission scanning electron microscopy.

Photoluminescence characterization

The PL spectrum was measured using an Edinburgh FLS1000 fluorescence spectrometer. The CIE chromaticity coordinates were calculated using CIE calculator software based on the emission spectra. The PLQY was acquired using an Edinburgh FLS980 fluorescence spectrometer equipped with a xenon lamp and a calibrated integrating sphere. PLQYs were calculated using the equation: $\eta_{QE} = I_S/(E_R - E_S)$, where I_S represents the luminescence emission spectrum of the sample, E_R is the spectrum of the excitation light from the empty integrated sphere (without the sample), and E_S is the excitation spectrum for exciting the sample. Time-resolved attenuation data were collected using the Edinburgh FLS980 fluorescence spectrometer and a picosecond pulsed diode laser.

Fabrication of WLED

The red $[AEP]Pb_{1-x}Mn_xCl_5 \cdot H_2O$ phosphor, commercial green phosphor of (Ba, Sr)SiO_4:Eu^{2+} (Shenzhen Looking Long Technology Co., Ltd, China), commercial blue phosphor of $BaMgAl_{10}O_{17}$:Eu^{2+} (Shenzhen Looking Long Technology Co., Ltd, China), and UV chip (365 nm, 3 V, 300 mA, Shenzhen Looking Long Technology Co., Ltd, China) were thoroughly mixed using an epoxy resin. The resulting mixture was then coated on the LED chip. The electrical and photoelectric properties, such as the emission spectrum, color temperature (CCT), color rendering index (R_a), and CIE color coordinates of the LED, were measured using an integrating sphere spectroradiometer system (EVERFINE HAAS-2000). The as-fabricated white LEDs were operated at 3 V with varied drive currents ranging from 20 to 120 mA.

Preparation of perovskite–PVP composites

To prepare the composites, 0.30 g of sample powder was dissolved in 1 mL of ethanol (EA) to obtain a homogeneous suspension solution. Next, 0.5 g of polyvinylpyrrolidone (PVP) was added to the solution and stirred at room temperature for 4 hours, resulting in a white viscous liquid. Finally, a thin film of $[AEP]Pb_{1-x}Mn_xCl_5 \cdot H_2O$ was obtained by spin-coating 50 μL of the viscous liquid onto a glass substrate at a speed of 2100 rpm.

Results and discussion

Crystal structure

Bulk single crystals of 1D $[AEP]PbCl_5 \cdot H_2O$ (**1**) were obtained through the facile solution evaporation method using 1-(2-aminoethyl)piperazine and $PbCl_2$ as precursors in hydrobromic acid (Fig. 1a). The single crystal structure of compound **1** was determined by X-ray single-crystal diffraction, and it crystallized in the monoclinic space group $P2_1/c$. The asymmetric unit of compound **1** comprises a 1D infinite zigzag $[PbCl_5]^{3-}$ chain, two $[AEP]^{3+}$ cations, and a guest water molecule. The octahedral

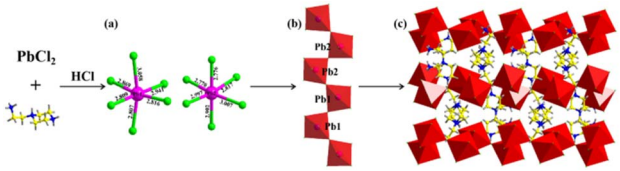

Fig. 1 Schematic diagram of the synthesis of $[AEP]PbCl_5 \cdot H_2O$ (**1**): (a) the coordination environments of $[PbCl_6]^{4-}$ units; (b) the structure of 1D $[PbCl_5]^{3-}$ chain; (c) the packing crystal structure of $[AEP]PbCl_5 \cdot H_2O$ viewed along the *c*-axis.

$[PbCl_6]$ structure exhibits slight distortion with the six Pb–Cl bond lengths ranging from 2.7713(10) to 3.05845(17) Å (Fig. 1b). The $Pb(1)Cl_6$ and $Pb(2)Cl_6$ units are interlinked by sharing two adjacent Cl atoms from each $[PbCl_6]$ octahedron to form a 1D zigzag chain, which is distinct from the approximately linear $[PbCl_5]^{3-}$ chain in $(2.6\text{-dmpz})_3Pb_2Cl_{10}$ (Fig. 1c).[40,41] The neighboring 1D $[PbCl_5]^{3-}$ chains stack closely in the [010] plane and are separated and surrounded by bulk $[AEP]^{3+}$ cations through weak N–H···Cl hydrogen bonds, forming a 3D H-bonding network. Consequently, this hybrid perovskite represents an ideal inorganic–organic hybrid phase, where 1D chains are individually encapsulated within a wide bandgap organic matrix. This unique structure allows the hybrid to exhibit distinct physical properties associated with the inorganic $[PbCl_5]^{3-}$ species. The powder X-ray diffraction (PXRD) pattern of the bulk crystals aligns with the simulation derived from single-crystal data, confirming the consistency of the crystal lattice and the high purity of the sample (Fig. S1†).

A series of $[AEP]Pb_{1-x}Mn_xCl_5 \cdot H_2O$ phases (compounds **2–8**) were synthesized by doping Mn^{2+} into compound **1**. The Mn^{2+}-doped compounds were systematically characterized using powder X-ray diffraction (PXRD), X-ray photoelectron spectroscopy (XPS), energy-dispersive X-ray spectroscopy (EDX), and elemental mapping. The PXRD patterns of the $[AEP]Pb_{1-x}Mn_xCl_5 \cdot H_2O$ series with varying Mn^{2+} concentrations are consistent with that of the undoped $[AEP]PbCl_5 \cdot H_2O$, indicating the same crystal structure without the presence of unwanted secondary phases. The diffraction peaks feature slight shift toward high angle with the increasing of Mn^{2+} content, which corresponds to lattice shrinkage and demonstrates success of Mn^{2+} doping (Fig. 2a). XPS analysis verifies the presence of C, N, Pb, and Cl elements, and the distinct peaks of Pb 4f, Cl 2p, C 1s, and N 1s orbitals suggest a single species for all components (Fig. 2b–f). The Mn $2p_{3/2}$ orbital energy is observed in the range of 641.05–645.95 eV, corresponding to the Mn^{2+} ion, which demonstrates the successful incorporation of Mn^{2+} ions into the 1D $[AEP]PbCl_5 \cdot H_2O$ structure (Fig. 2g). Furthermore, the EDX analysis indicates that the Mn element has been successfully doped into compound **1** (Fig. S2†).

The elemental mapping images further reveal that the elements C, N, Mn, Pb, and Cl are homogeneously distributed on the surface of the doped phase, confirming the composition uniformity (Fig. 2h). Following comprehensive characterization, it has been established that Mn^{2+} has successfully replaced a portion of Pb^{2+} in $[AEP]PbCl_5 \cdot H_2O$, leading to the formation of

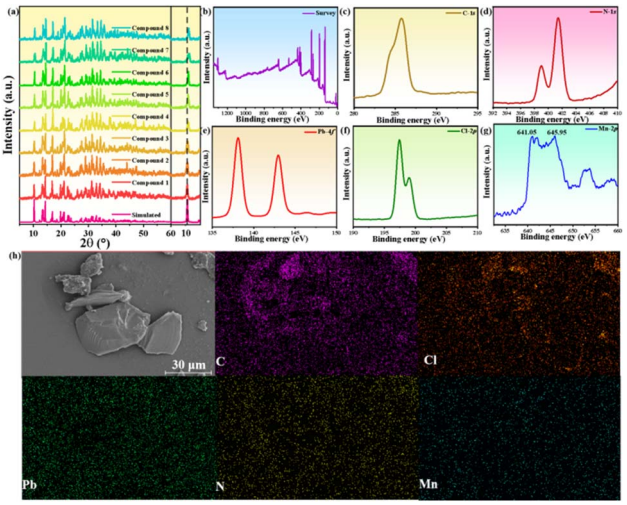

Fig. 2 Characterizations of Mn^{2+}-doped [AEP]$PbCl_5 \cdot H_2O$: (a) normalized XRD patterns; (b–g) XPS spectra; (h) SEM elemental mapping images of C, N, Pb, Cl and Mn for compound **8**.

a doped 1D perovskite with tunable Mn^{2+} concentrations (Fig. S3†). Notably, this doped perovskite retains an identical crystal structure and uniform elemental distribution, offering an exceptional structural platform for investigating the dynamic photophysical properties of the Mn^{2+}-doped 1D perovskite.

Luminescence properties

The luminescence properties of compound **1** were investigated using solid-state absorption, steady-state photoluminescence (PL) excitation and emission, and time-resolved spectroscopy at 300 K. The absorption spectrum of compound **1** exhibits a strong excitonic peak in the range of 200–350 nm (Fig. S4†). Under 365 nm UV light irradiation, bulk crystals of 1D [AEP]$PbCl_5 \cdot H_2O$ emit a faint blue-white light, similar to previous reports (Fig. 3a).[42] The PL excitation spectrum features a sharp peak at 360 nm, which is close to the maximum absorption peak of compound **1**, indicating intrinsic excitonic emission. Upon 365 nm UV light excitation, compound **1** emits a broadband blue-white light with a single maximum at 463 nm, wide full-width at half-maximum (FWHM) of 152.9 nm, large Stokes shift of 103 nm, and CIE chromaticity coordinates of (0.254, 0.303) (Fig. 3b and c). The weak blue-white light emission is verified by the measured PLQY of less 1% (Fig. S5†). The PL decay curve monitored at 463 nm gives an average lifetime of 1.36 ns at 300 K (Fig. 3d).

The emission color of the compound **1** changes from faint blue-white to bright orange-red under UV light illumination as Mn^{2+} is continuously doped (Fig. 4a). As the Mn^{2+} content increases, the compounds exhibit broad absorption bands in the 400–550 nm range, which is attributed to the electron transition within d^5 orbitals of Mn^{2+} ions (Fig. S4†). The steady-state PL emission spectra showed a red-shift to the dominant emission wavelength from 466 nm to 630 nm with increasing Mn^{2+} addition (Fig. 4b). The luminescence transformation from blue-white (0.20, 0.22) to red light (0.59, 0.36) is evident in the CIE chromaticity coordinates (Fig. 4c). To evaluate emission intensity and energy-transfer efficiency, we measure the PLQYs of serial Mn^{2+}-doped [AEP]$PbCl_5 \cdot H_2O$ (Fig. S5†). The PLQY increases monotonously to 8.96% as the Mn^{2+} content increases up to 3.13% (Fig. 4d). After elevating the dopant concentration to 4.62%, the emission intensity began to decline resulting from the concentration quenching effect triggered by the non-radiative energy transfer between the dopants. The critical distance between the adjacent dopants can be employed to justify the concentration quenching mechanism and it can be calculated through the following expression:[43]

$$R_c = 2\left(\frac{3V}{4\pi x_c Z}\right)^{1/3}, \quad (1)$$

where R_c, V, x_c, and Z describe the critical distance, volume of unit cell, critical doping content, and the amount of host cations in the unit cell, respectively. In this case, the values of V, x_c, and Z were 3050.3, 0.0313, and 4, respectively. Utilizing eqn (1), one finds that the critical distance of Mn^{2+} ions in the

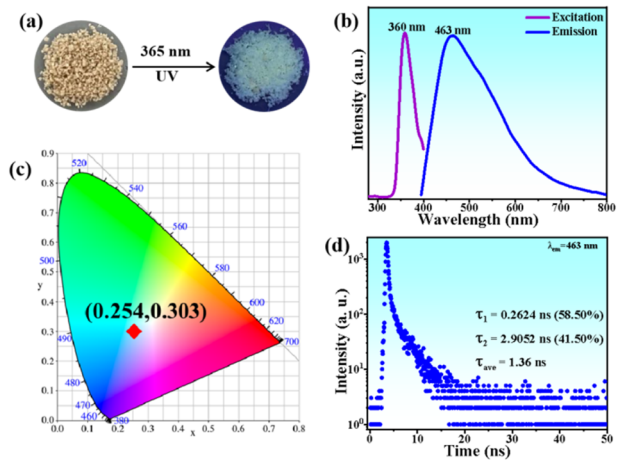

Fig. 3 PL characterizations of compound **1** at 300 K: (a) photo images of bulk crystals under ambient light and UV light; (b) excitation and emission spectra; (c) Commission Internationale de l'Eclairage (CIE) chromaticity coordinates; (d) PL decay curve monitored at 463 nm.

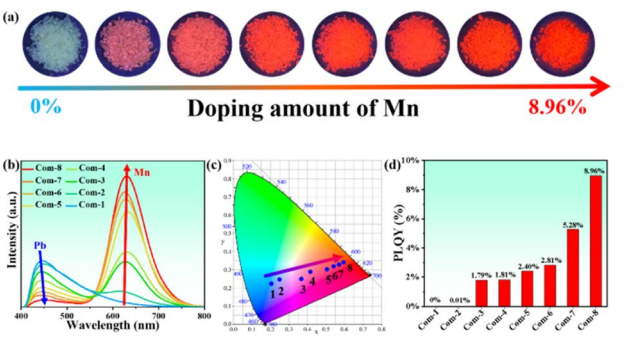

Fig. 4 PL characterizations of serial Mn^{2+}-doped [AEP]$PbCl_5 \cdot H_2O$ at 300 K: (a) photo images of bulk crystals under UV light; (b) consecutive tunable PL emission spectra; (c) CIE chromaticity coordinates, and (d) PLQYs for selected compounds **1**–**8**.

compound **9** was 35.97 Å. Usually, the concentration quenching mechanism will be contributed by the exchange interaction when the critical distance between the dopants is less than 5 Å, otherwise, it will be pertained by the multipole–multipole interaction when $R_c > 5$ Å. As the critical distance of Mn^{2+} ions in the compound **9** host lattice were much larger than 5 Å, it is reasonable to conclude that the multipole–multipole interaction would contribute to the aforementioned concentration quenching mechanism. Time-resolved PL decay curve monitoring at 619 nm is fitted with a double-exponential function, yielding an average lifetime of 0.2879 μs for compound **8** (Fig S6†).

According to the PXRD patterns, the crystal structure of Mn^{2+}-doped 1D [AEP]$PbCl_5 \cdot H_2O$ were not changed (Fig. 5a and d). According the band structure and density of state by DFT calculation (Fig. 5b–f), the redshift of PL emission of Mn^{2+}-doped 1D [AEP]$PbCl_5 \cdot H_2O$ is mainly due to the energy transfer between the host material and Mn^{2+} ions, and the increased incorporation of Mn^{2+} ions into the lattice. When Mn^{2+} ions are introduced into the 1D [AEP]$PbCl_5 \cdot H_2O$ lattice, they act as dopants and occupy the Pb^{2+} sites. This substitution leads to the formation of Mn^{2+}-related energy levels within the host material's bandgap (Fig. 5f). The energy transfer between the host lattice and Mn^{2+} ions, often referred to as Förster Resonance Energy Transfer (FRET), plays a crucial role in the observed redshift. This energy transfer process involves the absorption of photons by the host lattice, followed by a non-radiative transfer of energy to the Mn^{2+} ions. The Mn^{2+} ions then relax back to their ground state, emitting photons at a lower energy (longer wavelength) than the initially absorbed photons. This phenomenon results in the observed redshift of the photoluminescence in the Mn^{2+}-doped 1D [AEP]$PbCl_5 \cdot H_2O$ material (Fig S6†).

As the concentration of Mn^{2+} ions increase, the probability of FRET occurring also increases. Consequently, the steady-state PL emission spectra exhibit a gradual redshift of the dominant emission wavelength from 463 nm to 630 nm with the increasing addition of Mn^{2+} precursor. Additionally, as the Mn^{2+} doping concentration increases, the local crystal field around the Mn^{2+} ions may change, further influencing the emission wavelength and causing a redshift. It is important to note that the energy transfer process can also lead to luminescence quenching if the Mn^{2+} doping concentration is too high. This is due to the increased likelihood of non-radiative relaxation processes taking place, which can reduce the overall photoluminescence quantum yield. In this study, the highest PLQY of 8.96% was achieved by optimizing the Mn^{2+} doping concentration to balance the redshift and emission intensity.

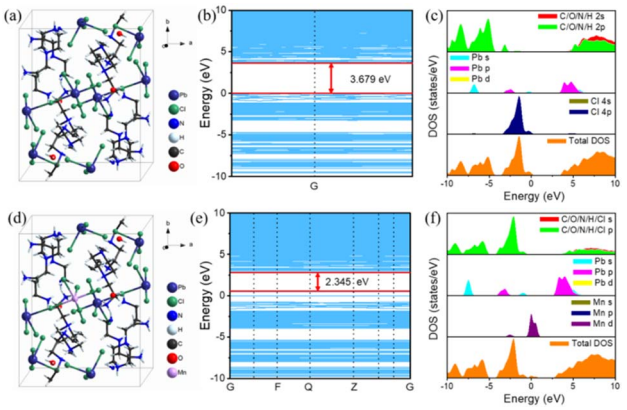

Fig. 5 DFT calculation for pristine and Mn^{2+}-doped 1D [AEP]$PbCl_5 \cdot H_2O$. (a) Unit cell structure, (b) the calculated band structures, and (c) the total and partial density of states for 1D [AEP]$PbCl_5 \cdot H_2O$. (d) Unit cell structure, (e) the calculated band structures, and (f) the total and partial density of states for Mn^{2+}-doped 1D [AEP]$PbCl_5 \cdot H_2O$.

Stability property

Stability is a crucial factor for luminescent perovskite materials in photoelectric applications, leading to extensive research in this area. After investigating the photoluminescence (PL) properties of compounds **1–8**, we focused on their structural and optical stability in various chemical and physical environments. To assess the stability of the samples in humid environments, we stored them in ambient air with a high humidity of 90% for two months. Comparing the PL emission spectra of compound **8** before and after storage, we found that the PL spectra remained consistent with nearly identical emission intensity (Fig. S7†). This suggests that these compounds exhibit good stability in humid environments.

We also studied the thermal stability of the perovskites, as optoelectronic devices often operate continuously at high temperatures. Thermogravimetric analysis revealed that these 1D perovskites could be stabilized below 160 °C (Fig. S8†). To further investigate their thermal stability, we analyzed the temperature-dependent PXRD patterns of samples after constant heating (Fig. S9 and S10†). The unchanged PXRD patterns and PL spectra indicate the sufficient thermal stability. We then prepared perovskite–PVP composites by mixing compound **8** and polyvinylpyrrolidone in ethanol, and the film was deposited by one-step spin-coating from the precursor solution (Fig. S11†). The deposited perovskite–PVP film showed excellent crystallization and emitted a bright orange-red light under UV excitation with a broadband emission spectrum similar to compound **8** (Fig. S11b–d†). The PXRD pattern of the deposited film matched the simulated result from single-crystal structural data, indicating a high degree of crystallization. In summary, the remarkable stability of compound **8** offers possibilities for its application in photoelectric performance.

Applications in solid-state LEDs

The successful assembly of various luminescent devices based on compound **8** has inspired us to further explore its application in solid-state LEDs. To demonstrate this performance, we fabricated a white LED by coating a mixture of red-light emitter (compound **8**) with commercial green ((Ba, Sr) SiO_4:Eu^{2+}) and blue ($BaMgAl_{10}O_{17}$:Eu^{2+}) phosphors on a 365 nm UV chip. Driven by a 20 mA current, the white LED device emits bright white light, further characterized by electroluminescence (EL) spectroscopy at room temperature (Fig. 6a). The EL emission spectrum spans the entire visible region, with CIE chromaticity

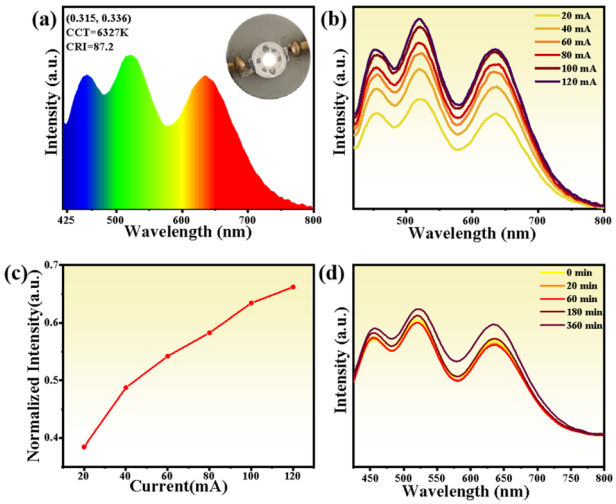

Fig. 6 (a) The PL spectra of the white LED fabricated using compound **8** at a 20 mA drive current (inset: photograph of the fabricated white LEDs); (b) drive current dependent PL spectra of the fabricated white LED device; (c) normalized peak intensity variation of the fabricated white LED under various operating currents; (d) operating time-dependent PL spectra of the fabricated white LED devices.

coordinates of (0.315, 0.336) and a correlated color temperature (CCT) of 6327 K, corresponding to "warm" white light. Moreover, even without precise control of the mixing ratio of the three phosphors, the broadband EL emission spectrum of the white LED achieves a high color rendering index (CRI) of 87.2, surpassing commercial white LEDs based on YAG:Ce^{3+} (CRI < 80). Operating current-dependent EL was further performed to evaluate the spectral stability of the white LED. The EL emission intensity steadily increases with the enhanced current from 20 to 120 mA, indicating the absence of energy transfer between different phosphors and potential application in high-power optoelectronic devices (Fig. 6b and c). Surprisingly, under constant drive for at least 360 minutes, the fabricated white LED still exhibits high emission intensity without significant reduction (Fig. 6d), further demonstrating the excellent thermal and optical stability of the fabricated white LED device.

Conclusions

In conclusion, we demonstrate the synthesis and characterization of Mn^{2+}-doped one-dimensional $[AEP]PbCl_5 \cdot H_2O$ hybrid lead halide perovskites. The incorporation of Mn^{2+} ions as dopants in the perovskite lattice leads to tunable photoluminescence properties, resulting in a redshift of the dominant emission wavelength. The optimized doping concentration yields an enhanced PLQY from less than 1% to 8.96%, making these materials promising candidates for optoelectronic applications. The structural and optical stability of the doped perovskites under humid and high-temperature conditions have been thoroughly investigated, revealing their excellent performance under adverse environmental conditions. The perovskite–PVP composite films also exhibit high crystallization and bright orange-red emission under UV excitation. Furthermore, a WLED device has been fabricated using the Mn^{2+}-doped perovskite in combination with commercial green and blue phosphors. The fabricated LED exhibits a high color rendering index of 87.2 and stable electroluminescence performance under various operating currents and extended operation times. This study highlights the potential of Mn^{2+}-doped one-dimensional hybrid lead halide perovskites as efficient and stable phosphors for high-performance white light emitting diodes and other optoelectronic applications.

Conflicts of interest

There are no conflicts to declare.

Acknowledgements

We express thanks for the financial supports from the National Nature Science Foundation of China (No. 22201099 and 21601104) and the Shandong Provincial Natural Science Foundation (ZR2021QB204).

References

1 H. B. Cho, J. W. Min, H. J. Kim, N. S. M. Viswanath, T. Samanta, J. H. Han, Y. M. Park, S. W. Jang and W. B. Im, *ACS Appl. Electron. Mater.*, 2023, **5**, 66–76.
2 J. K. Meyers, S. Kim, D. J. Hill, E. E. M. Cating, L. J. Williams, A. S. Kumbhar, J. R. McBride, J. M. Papanikolas and J. F. Cahoon, *Nano Lett.*, 2017, **17**, 7561–7568.
3 C. Xie, C. K. Liu, H. L. Loi and F. Yan, *Adv. Funct. Mater.*, 2020, **30**, 1903907.
4 J. Y. Li, Z. Y. Han, Y. Gu, D. J. Yu, J. X. Liu, D. W. Hu, X. B. Xu and H. B. Zeng, *Adv. Funct. Mater.*, 2021, **31**, 2008684.
5 S. Y. Zhao, W. S. Cai, H. X. Wang, Z. G. Zang and J. Z. Chen, *Small Methods*, 2021, **5**, 2001308.
6 W. Ma, J. L. Yin, X. F. Chen, C. Sun, X. L. Song and H. H. Fei, *Chem. Mater.*, 2022, **34**, 4403–4413.
7 F. F. Gao, X. Li, Y. Qin, Z. G. Li, T. M. Guo, Z. Z. Zhang, G. D. Su, C. Y. Jiang, M. Azeem, W. Li, X. Wu and X. H. Bu, *Adv. Opt. Mater.*, 2021, **9**, 2100003.
8 J. H. Fan, Y. Qin, M. Azeem, Z. Z. Zhang, Z. G. Li, N. Sun, Z. Q. Yao and W. Li, *Dalton Trans.*, 2021, **50**, 2648–2653.
9 S. Mukherjee, J. Selvaraj and T. Paramasivam, *ACS Appl. Nano Mater.*, 2021, **4**, 10228–10243.
10 I. Lignes, R. M. Maceiczyk, M. V. Kovalenko and S. Stavrakis, *Chem. Mater.*, 2020, **32**, 27–37.
11 P. Vashishtha, S. Bishnoi, C. H. A. Li, M. Jagadeeswararao, T. J. N. Hooper, N. Lohia, S. B. Shivarudraiah, M. S. Ansari, S. N. Sharma and J. E. Halpert, *ACS Appl. Electron. Mater.*, 2020, **2**, 3470–3490.
12 F. Palazon, F. D. Stasio, Q. A. Akkerman, R. Krahne, M. Prato and L. Manna, *Chem. Mater.*, 2016, **28**, 2902–2906.
13 K. Hong, Q. V. Le, S. Y. Kim and H. W. Jang, *J. Mater. Chem. C*, 2018, **6**, 2189–2209.
14 H. Peng and B. S. Zou, *J. Phys. Chem. Lett.*, 2022, **13**, 1752–1764.

15 C. Y. Yue, C. Sun, D. Y. Li, Y. H. Dong, C. L. Wang, H. F. Zhao, H. Jiang, Z. H. Jing and X. W. Lei, *Inorg. Chem.*, 2019, **58**, 10304–10312.
16 Y. L. Mao, J. Zhang, Q. Q. Ren, M. S. Molokeev, G. J. Zhou and X. M. Zhang, *J. Mater. Chem. C*, 2022, **10**, 17638–17645.
17 Y. Han, S. J. Yue and B. B. Cui, *Adv. Sci.*, 2021, **8**, 2004805.
18 H. M. Cheng, C. Cao, S. Y. Teng, Z. N. Zhang, Y. Zhang, D. Y. Wang, W. S. Yang and R. G. Xie, *Dalton Trans.*, 2023, **52**, 1021–1029.
19 Y. L. Jiang, J. l. Yin and H. H. Fei, *J. Mater. Chem. C*, 2022, **10**, 13254–13261.
20 Y. C. Peng, H. W. Lin, S. H. Zhou, J. C. Jin, T. H. Zhuang, A. Ablez, Z. P. Wang, K. Z. Du and X. Y. Huang, *Molecules*, 2023, **28**, 1978.
21 H. M. Yang, J. L. Yin, X. X. Xu and H. H. Fei, *J. Mater. Chem. C*, 2019, **7**, 7090–7095.
22 Y. C. Peng, S. H. Zhou, J. C. Jin, Q. Gu, T. H. Zhuang, L. K. Gong, Z. P. Wang, K. Z. Du and X. Y. Huang, *Dalton Trans.*, 2022, **51**, 4919–4926.
23 C. Q. Jing, X. Yin, P. C. Xiao, Y. J. Gao, X. M. Wu, C. Y. Yue and X. W. Lei, *Chem.–Eur. J.*, 2022, **28**, e202103043.
24 P. Arunkumar, K. H. Gil, S. Won, S. Unithrattil, Y. H. Kim, H. J. Kim and W. B. Im, *J. Phys. Chem. Lett.*, 2017, **8**, 4161–4166.
25 L. Hou, Y. H. Zhu, J. R. Zhu, X. Y. Li, F. Zeng, T. Y. Yang, Y. Q. Gong, J. H. Shen and C. Z. Li, *Adv. Mater. Interfaces*, 2021, **8**, 2002175.
26 A. Biswas, R. Bakthavatsalam and J. Kundu, *Chem. Mater.*, 2017, **29**, 7816–7825.
27 S. K. Dutta, A. Dutta, S. D. Adhikari and N. Pradhan, *Chem. Mater.*, 2017, **29**, 7816–7825.
28 R. Bakthavatsalam, A. Biswas, M. Chakali, P. R. Bangal, B. P. Kore and J. Kundu, *J. Phys. Chem. C*, 2019, **123**, 4739–4748.
29 Y. J. Guo, J. Su, L. Wang, Z. H. Lin, Y. Hao and J. J. Chang, *J. Phys. Chem. Lett.*, 2021, **12**, 3393–3400.
30 K. Xing, X. Yuan, Y. Wang, J. Li, Y. J. Wang, Y. Fan, L. Yuan, K. Li, Z. J. Wu, H. B. Li and J. L. Zhao, *J. Phys. Chem. Lett.*, 2019, **10**, 4177–4184.
31 M. H. P. Usman, R. Bakthavatsalam and J. Kundu, *ChemistrySelect*, 2018, **3**, 6585–6595.
32 W. V. D. Stam, J. J. Geuchies, T. Altantzis, K. H. W. V. D. Bos, J. D. Meeldijk, S. V. Aert, S. Bals, D. Vanmaekelbergh and C. D. M. Donega, *J. Am. Chem. Soc.*, 2017, **139**, 4087–4097.
33 C. K. Zhou, Y. Tian, O. Khabou, M. Worku, Y. Zhou, J. Hurley, H. R. Lin and B. W. Ma, *ACS Appl. Mater. Interfaces*, 2017, **9**, 40446–40451.
34 A. K. Guria, S. K. Dutta, S. D. Adhikari and N. Pradhan, *ACS Energy Lett.*, 2017, **2**, 1014–1021.
35 D. Ricciarelli, D. Meggiolaro, P. Belanzoni, A. A. Alothman, E. Mosconi and F. D. Angelis, *ACS Energy Lett.*, 2021, **6**, 1869–1878.
36 G. J. Zhou, X. F. Jia, S. Q. Guo, M. Molokeev, J. Y. Zhang and Z. G. Xia, *J. Phys. Chem. Lett.*, 2019, **10**, 4706–4712.
37 Z. J. Li, E. Hofman, A. H. Davis, A. Khammang, J. T. Wright, B. Dzikovski, R. W. Meulenberg and W. W. Zheng, *Chem. Mater.*, 2018, **30**, 6400–6409.
38 W. Y. Liu, Q. L. Lin, H. B. Li, K. F. Wu, I. Robel, J. M. Pietryga and V. I. Klimov, *J. Am. Chem. Soc.*, 2016, **138**, 14954–14961.
39 D. Parobek, B. J. Roman, Y. Dong, H. Jin, E. Lee, M. Sheldon and D. H. Son, *Nano Lett.*, 2016, **16**, 7376–7380.
40 M. B. H. Salah, N. Mercier, M. Allain, N. Zouari and C. Botta, *J. Mater. Chem. C*, 2019, **7**, 4424–4433.
41 S. A. Fateev, A. A. Petrov, E. I. Marchenko, Y. V. Zubavichus, V. N. Khrustalev, A. V. Petrov, S. M. Aksenov, E. A. Goodilin and A. B. Tarasov, *Chem. Mater.*, 2021, **33**, 1900–1907.
42 J. Q. Zhao, C. Sun, M. Yue, Y. Meng, X. M. Zhao, L. R. Zeng, G. Chen, C. Y. Yue and X. W. Lei, *Chem. Commun.*, 2021, **57**, 1218–1221.
43 P. Du, L. H. Luo and W. Cheng, *J. Am. Ceram. Soc.*, 2019, 1–7.